ANALYSIS OF ADJOINT FLUX CALCULATION FOR DETECTOR RESPONSE ESTIMATION IN TYPICAL PWR CONDITIONS

A Thesis Presented for the

Master of Science

Degree

The University of Tennessee, Knoxville

Shane Christopher Henderson

August 2019

This is dedicated to my loving wife and kids for their inexhaustible patience and support. Thank you so much!

ACKNOWLEDGEMENTS

I am deeply grateful to my advisor, Kevin Clarno, for his mentorship and guidance. Most importantly I would like to thank him for providing the opportunity to be a part of the CASL team, my experiences at ORNL has advanced my education as much as any classroom. I would also like to thank the remainder of my thesis committee, Ivan Maldonado and Ronald Pevey, for their help in completing this thesis. A special thanks goes out to Andrew Godfrey, Katherine Royston, Eva Davidson, Tara Pandya, and Ben Collins for all their help throughout the process of developing this work. Finally thank you to all the CASL PHI and EXCORE teams for all their contributions in making this work.

This research was supported by the Consortium for the Advanced Simulation of Light Water Reactors (www.casl.gov), an Energy Innovation Hub (http://www.energy.gov/hubs) for Modeling and simulation of Nuclear Reactors under U.S. Department of Energy Contract No. DE-AC05-00OR22725.

ABSTRACT

Reactor power is sensed by ex-core instrumentation by measuring the core neutron leakage. The measured magnitude of this leakage is sensitive to the conditions in which the reactor is operating. By being able to accurately estimate the neutron flux which will reach the detector position we can accurately estimate the power level and power distribution for a variety of operating conditions. The analysis presented here seeks to establish a minimum parameter set for solving an adjoint reactor problem at given conditions which can then be used to estimate the response using the forward solution at a different set of conditions. This type of estimation can be utilized for determining detector placement, detector design, and detector calibration procedures. Further extensions can be utilized in establishing conservative criteria for core protective actions.

TABLE OF CONTENTS

LIST OF TABLES

LIST OF FIGURES

1. INTRODUCTION

Continuous safe reactor operations are guaranteed through continuous monitoring of core power level and power distribution. The data collected via the various power instrumentation provides input for operators and automated protection systems, both of which work to ensure that safety limits are not violated. To do this requires reliable instruments and an understanding on how the instruments will respond under the wide range of possible conditions.

This work aims to detail methods for accurately and efficiently estimating detector response given a set of operating conditions. Since establishing the fission source is the driving factor of detector response, this work will consider a weighted core power distribution in its formulation. This is not unlike what other have previously explored.

However, this work will account for a variety of conditions in formulating the weights and will rely on rigorously constructing these weights, instead of utilizing manually ascribed weights as in some literature. By forming the weights in a methodical and programmatic way, the sensitivity of the weights to changing conditions can be explored which will enable generating fitting schemes and or condition-based corrections. These modified weights can then be used to accurately model detector response for a variety of conditions and powers distributions, while maintaining a defined bound on the error.

1.1. Power Monitoring

In principle, it is possible to measure the total output of an operating reactor using calorimetric techniques. For pressurized water reactors this can be done by carefully measuring temperatures and flow rates on either the primary or secondary loops. However, the thermodynamic relations that make this an accurate method, require that the reactor be operating at steady state. As such these methods are invalid during any type of transient, including start-ups and power maneuvers. Calorimetric studies also require significant resources to monitor and record all the various parameters of the study and are unable to describe the detailed power distribution within the core. This makes calorimetry a useful tool for establishing known reference powers but makes it completely infeasible for continuous monitoring.

Since it is not practical to measure reactor power directly, reactor power must be monitored through other means. This is commonly done by utilizing a neutron sensitive material to interact with the neutron flux in and around the core. These interactions then generate charged particles which can be utilized to induce an electrical current proportional to the neutron flux at that location. Since most free neutrons are a result of fission, the measured flux is proportional to the reactor power. Since most materials have much higher thermal neutron interaction probabilities (cross-sections), electrical signal from fast neutron interactions is typically insignificant. Designing detectors to have more favorable fast neutron detection properties is possible, but since PWRs have ample moderating capacity discussion of such designs is beyond the present scope.

1.1.1. In-core Instruments

Measuring the neutron flux within the reactor is a natural choice for establishing the output power and power distribution of a reactor. Several designs exist for obtaining such information, but the simplest are fixed in location and provide an indication for the integral flux over their length. This necessitates installing detectors of various lengths into the locations of concern to provide indications from which useful information can be deduced. Slightly more complicated than fixed detectors are moveable in-core detectors. These instruments can measure fluxes at locations approximating points throughout the instrument tube.

Regardless of type there is an inherent disadvantage in this approach. Pins that are further away from the detector are shadowed by the nearby pins. Therefore, signals obtained from in-core detectors are dominated by pins local to the detector [1]. This then requires an array of in-core detectors to infer the full power shape. Because of this, the failure of a single instrument can cause a substantial reduction in the observable power distribution.

1.1.2. Ex-core Detectors

In contrast, ex-core nuclear instruments measure the neutron leakage from the reactor periphery. Because of the large number of fission reactions occurring the leaked flux can be considered directly proportional to the number of fissions within the core. Since the power is directly proportional to the number of fissions, then the signal generated by the ex-core detector is proportional to the total power generated. It is worth noting that while the ex-core detector itself predominately interacts with thermal neutrons, most of the neutrons that reach the detector are leaked at much higher energies. It is also worth noting that this isn't entirely dissimilar from in-core instruments, except that the ex-core signal is dominated by the nearest assemblies rather than the nearest pins.

Not unlike in-core flux, the ex-core flux spans many orders of magnitude, coupling this with the physical distance between the core and ex-core detectors typically requires 3 different ex-core detector designs to cover the full range. These include the so-called source range (SR), intermediate range (IR), and power range (PR) instruments. It is worth noting that the SR and IR instruments are typically biased to reduce the contribution of gamma rays to the power signal [1]. While PR instruments typically do not require compensation, in part this is because the neutron signal is so strong, but also because the gamma signal is also proportional to power level in the PR [1].

While the response of the instrument is proportional to the neutron population that leaks to that position, it cannot be considered unique to a single power distribution. For this reason, pairs of detectors, top and bottom, are arranged 90 degrees radially from each other. This results in 8 detectors being positioned around the core, and the integral of their respective signals at full power, based on calorimetry, is considered to represent 100% power [1].

From this reference point many things can be inferred, most notably it defines observable power indication for operators. When the data is combined with the signals from the array of in-core detectors, the axial offset and radial power tilt can be defined and observed to change during operation. Coupling this with input for temperature and flow enables setting protective actions based on high-powered assemblies. While this methodology has been demonstrated as robust and proven reliable for existing designs, advanced reactor designs may require further consideration to ensure continued safe operation. This then requires efficient estimation of detector responses across a range of conditions to quickly study the multitude of advanced concepts as they emerge.

1.1.3. Current Practice

The baseline for calibrating ex-core detectors required direct comparison of ex-core detector responses to in-core detector data. This was enabled via linear regression or a “multi-point methodology”. To perform this calibration operators first induce an axial xenon transient. Then during this transient the flux is mapped over several radial and axial positions via in-core instruments. This could then be used to ascertain the point at which there was no axial tilt and from this a gain could be added or subtracted from the ex-core signals to reproduce the axial power information that was produced via in-core instrumentation [2]. While this provides generally reliable results, it is time consuming and often requires reduced power operations to prevent violating limits.

An alternate method of correlating the in-core power shape to the ex-core responses was explored by Shimazu [2]. In this approach it was surmised that the in-core data could be weighted to create an effective neutron source at the surface of the reactor vessel. This effective source could then be treated as an isotropic source at each node along the surface of the vessel. This enabled the generation of a single parameterized equation that could be used to calculate the contribution to response from each node, and subsequently the sum of contributions or total response. This method is effective in being able to treat the responses of each detector from the single source, however it does require determination of the "effective neutron removal" between the vessel and detector [2].

1.2. Literature Search

A search of open literature reveals little on investigating the efficiency or validity of ex-core detector response estimation. Of the works reviewed the most notable are presented here.

A study by Farkas, Lipka, et al. sought to calculate ex-core detector weighting functions for VVERs using MCNP. In this work, the authors utilized established manual variance reduction techniques to generate weights for each pin and then functionalize these weights into a polynomial. In many regards, it seems they met with success in generating the polynomials they sought but the paper itself lacked adequate comparison data to validate results. Though their work did corroborate the common conception that the outermost assemblies provide a disproportionately high contribution to detector response [3].

Zheng, Lee, et al. sought to compare a deterministic and stochastic method for ex-core detector response. The logic used for their work was utilized in forming the basis for the present work. However, their applications again focused on the comparison between software methodologies for what seems to be a single parameter set. Though they were able to generate good agreement between the methods, they also had significant differences in some data sets and the explanation of those difference informed the present work as well [4].

1.3. Modeling Software

For this study the Virtual Environment for Reactor Applications (VERA) developed by the Consortium for Advanced Simulation of LWRs (CASL) will be utilized. VERA provides a full suite of applications aimed at simulating reactor operation. One application in VERA provides a coupled deterministic-stochastic methodology utilizing MPACT to solve the fission source and Shift to perform the ex-core transport [5].

1.4. MPACT

MPACT implements method-of-characteristics (MOC) to solve the Boltzmann transport equation for practical three-dimensional (3D) reactors with sub-pin power resolution [6].

1.4.1. Method of Characteristics

The implementation first considers the Boltzmann transport equations in steady state continuous form.

$$\begin{aligned} &\Omega \cdot \nabla\psi(r,\Omega,E) + \Sigma_t(\mathrm{r},\Omega,\mathrm{E})\psi(\mathrm{r},\Omega,\mathrm{E}) \\ &= \frac{\chi(E)}{4\pi k_{eff}} \int_0^\infty \nu\Sigma_f(r,\Omega,E') \int_0^{4\pi} \psi(r,\Omega',E') \mathrm{d}\Omega'\, \mathrm{d}E' \\ &+ \int_0^\infty \int_0^{4\pi} \Sigma_s(r,\Omega'\cdot\Omega,E'\to E)\psi(r,\Omega',E')\mathrm{d}\Omega' \mathrm{d}E'. \end{aligned} \tag{1}$$

Which is often condensed by defining a source term for the right-hand side

$$\begin{aligned} q(r,\Omega,E) = &\frac{\chi(E)}{4\pi k_{eff}} \int_0^\infty \nu\Sigma_f(r,\Omega,E') \int_0^{4\pi} \psi(r,\Omega',E')\, \mathrm{d}\Omega' \mathrm{d}E' \\ &+ \int_0^\infty \int_0^{4\pi} \Sigma_s(r,\Omega'\cdot\Omega,E'\to E)\psi(r,\Omega',E')\mathrm{d}\Omega'\, \mathrm{d}E' \end{aligned} \tag{2}$$

yielding,

$$\Omega \cdot \nabla\psi(r,\Omega,E) + \Sigma_t(\mathrm{r},\Omega,\mathrm{E})\psi(\mathrm{r},\Omega,\mathrm{E}) = q(r,\Omega,E). \tag{3}$$

Then applying method of characteristics, transforms the spatial and angular components to variables along the characteristic.

$$\mathrm{r} = r_o + \mathrm{s}\Omega \Rightarrow \begin{aligned} x_s &= x_o + \mathrm{s}\Omega_x \\ y_s &= y_o + s\Omega_y \\ z_s &= z_o + \mathrm{s}\Omega_z \end{aligned}$$

From here the characteristic form of equation (1) is obtained

$$\frac{\mathrm{d}\psi}{\mathrm{ds}}(\mathrm{r_o} + \mathrm{s}\Omega,\Omega,\mathrm{E}) + \Sigma_t(\mathrm{r_o} + \mathrm{s}\Omega,\mathrm{E})\psi(\mathrm{r_o} + \mathrm{s}\Omega,\Omega,\mathrm{E}) = \mathrm{q}(\mathrm{r_o} + \mathrm{s}\Omega,\Omega,\mathrm{E}), \tag{4}$$

where equation (2) now takes the form

$$
\begin{aligned}
&\mathrm{q}(r_o + \mathrm{s}\Omega, \Omega, \mathrm{E}) \\
&= \frac{\chi(r_o + \mathrm{s}\Omega, E)}{4\pi k_{eff}} \int_0^{\infty} \int_0^{4\pi} \nu\Sigma_f(r_o + \mathrm{s}\Omega', \Omega', E')\psi(r_o + \mathrm{s}\Omega', \Omega', E')\mathrm{d}\Omega'\, \mathrm{d}E' \\
&+ \int_0^{\infty} \int_0^{4\pi} \Sigma_s(r_o + \mathrm{s}\Omega, \Omega' \cdot \Omega, E' \to E)\psi(r_o + \mathrm{s}\Omega', \Omega', E')\, \mathrm{d}\Omega' \mathrm{d}\, E'.
\end{aligned} \tag{5}
$$

This can then be solved by use of the integrating factor

$$
exp\left(- \int \Sigma_t(r_o + s'\Omega, E)\mathrm{d}s'\right),
$$

resulting in

$$
\begin{aligned}
&\psi(r_o + s\Omega, \Omega, E) \\
&= \psi(r_o, \Omega, E)\, \exp\left(- \int_{\mathrm{o}}^{\mathrm{s}} \Sigma_t(r_o + s'\Omega, E)\mathrm{d}s'\right) \\
&+ \int_0^{s} \mathrm{q}(r_o + s'\Omega, \Omega, E)\exp\left(- \int_{\mathrm{s}'}^{\mathrm{s}} \Sigma_t(r_o + s''\Omega, E)\mathrm{d}s''\right)\mathrm{d}\, \mathrm{s}'.
\end{aligned} \tag{6}
$$

The final equation is then discretized for numerical solution [6].

1.4.2. Discretization

Various discretization techniques have been developed for solving the many differential and integral equations that occur in physics. For steady state neutron transport variables for space, angle, and energy must be discretized before numerically solving.

1.4.2.1. Multigroup Approximation

The multigroup approximation discretizes neutron energy by defining energy bands called groups. Since all neutron cross sections have energy dependence, forming these groups requires collapsing the continuous energy cross sections into groups while preserving reaction rates. This can be accomplished exactly by the following

$$
\Sigma_{x,g}(r) = \frac{\int_{E_g}^{E_{g-1}} \Sigma(r, E)\psi(r, \Omega, E)\mathrm{d}\, E}{\int_{E_g}^{E_{g-1}} \psi(r, \Omega, E)\mathrm{d}\, E}. \tag{7}
$$

However, the angular flux distribution is typically one of the unknows being solved and is therefore unknown prior to the discretization. Therefore, it is necessary to make an approximation of the form

$$\psi(r,\Omega,E) \approx \varphi(r,E) f(r,\Omega),$$

which forms the following

$$\Sigma_{x,g}(r) \approx \frac{\int_{E_g}^{E_{g-1}} \Sigma(r,E)\varphi(r,\Omega,E)\mathrm{d}E}{\int_{E_g}^{E_{g-1}} \varphi(r,\Omega,E)\mathrm{d}E}. \tag{8}$$

This works for everything but the fission spectrum which is a probability more than a cross section. Therefore, it can simply be found as

$$\chi_{\mathrm{g}}(r) = \int_{E_g}^{E_g-1} \chi(r,E)\mathrm{d}\,E. \tag{9}$$

This operation is generally done external to MPACT and the resulting cross section library is supplied as an input [6].

1.4.2.2. Discrete Ordinates

This approximation discretizes the angular component of the transport equation and is typically implemented as a quadrature of the following form

$$\int_{4\pi} f(\Omega)\mathrm{d}\Omega \approx \sum_{m=1}^{M} w_m f(\Omega_m).$$

Several quadratures exist but in general applying one to equation (6) results in

$$\begin{aligned}\psi_{\mathrm{g,m}}(\mathrm{r_o} + \mathrm{s}\Omega_{\mathrm{m}}) &= \psi_{\mathrm{g,m}}(\mathrm{r_o})\exp\left(-\int_0^s \Sigma_{t,g}(r_o + s'\Omega_m)\mathrm{d}s'\right) \\ &+ \int_0^s q_{g,m}(r_o + s'\Omega_m) exp\left(-\int_{s'}^s \Sigma_{t,g}(r_o + s''\Omega_{\mathrm{m}}) ds''\right) ds'.\end{aligned} \tag{10}$$

Where the source term is now

$$q_{g,m}(r_o + s\Omega_m, E) = \frac{\chi_g(r_o + s\Omega_m)}{4\pi k_{eff}} \sum_{g'=1}^{G} \sum_{m'}^{M} \nu\Sigma_{f,g'}(r_o, s\Omega_m) w_{m'} \psi_{g',m'}(r_o + s\Omega_{m'}) + \sum_{g'=1}^{G} \sum_{m'}^{M} \Sigma_{s,g'\to g}(r_o, s\Omega_{m'}, \Omega_{m'} \cdot \Omega_m) w_{m'} \psi_{g',m'}(r_o + s\Omega_{m'}). \tag{11}$$

While it is known that making this approximation results in the introduction of some error, the discrete ordinates method has been shown to be accurate in most cases. For difficult problems experimentation with the order of the ordinates has been shown to improve reliability [6].

1.4.2.3. *Constant Properties*

MPACT like many other neutronics codes, relies on each discretized region having a flat source distribution across its volume. In simple terms this requires that the flux and all material properties be static within each discrete region [6]. Which allows for solving the integrals and reducing equation (10) to the following

$$\psi_{i,g,m,k}^{out} = \psi_{i,g,m,k}^{in} exp\left(-\Sigma_{t,i,g} s_{i,m,k}\right) + \frac{q_{i,g,m}}{\Sigma_{t,i,g}}\left[1 - exp\left(-\Sigma_{t,i,g} s_{i,m,k}\right)\right], \tag{12}$$

where the source term is now

$$q_{i,g,m} = \frac{\chi_{i,g}}{4\pi k_{eff}} \sum_{g'=1}^{G} \nu\Sigma_{f,g'} \sum_{m'}^{M} w_{m'} \psi_{g',m'} + \sum_{g'=1}^{G} \sum_{m'}^{M} \Sigma_{s,g'\to g}(\Omega_{m'} \cdot \Omega_m) w_{m'} \psi_{g',m'}. \tag{13}$$

This final equation can then be iterated over to obtain solutions for the flux and effective multiplication factor.

1.5. Shift

Shift provides VERA with a production level continuous energy stochastic transport capability. This gives VERA a high-fidelity transport tool that does not rely on space, angle, or energy discretization [7].

1.5.1. Coupling

MPACT and Shift both initialize from the VERA common input and allows users to solve the reactor and ex-core problems in tandem. While Shift has a built-in eigenvalue solver, this study is primarily interested in its ex-core transport capability. The implementation for this allows the user to specify a fission source, or when coupled to MPACT, utilize the MPACT fission source as the basis for sampling particles. This is accomplished by treating the fission distribution as an un-normalized probability density function (pdf). This pdf defines the probability that a particle will be born at a location and is used for generating the neutrons that will be used in the stochastic transport. This coupling significantly improves the usability and applicability of VERA to this type of problem and ensures both codes solve on common conditions [7].

1.5.2. CADIS

Shift also provides powerful variance reduction support through the consistent adjoint driven importance sampling (CADIS) method [7]. Starting with equation (1) the CADIS method developed by Wagner and Haghighat can be derived utilizing the adjoint property

$$\langle \psi^*, H\psi \rangle = \langle \psi, H^*\psi^* \rangle \tag{14}$$

and where H and H^* are the forward and adjoint operators defined by

$$\mathrm{H} = \Omega \cdot \nabla + \Sigma_{\mathrm{t}}(\mathrm{r}, \mathrm{E}) - \int_0^\infty \int_{4\pi} \Sigma_s(r, E' \to E, \Omega' \to \Omega) \mathrm{d}\Omega dE^{'} \tag{15}$$

$$H^* = -\Omega \cdot \nabla + \Sigma_{\mathrm{t}}(\mathrm{r}, \mathrm{E}) - \int_0^\infty \int_{4\pi} \Sigma_s(r, E \to E', \Omega \to \Omega') \mathrm{d}\Omega dE^{'} . \tag{16}$$

This leads to the following

$$\mathrm{H}\psi = \mathrm{q} \text{ in } \mathrm{V} \tag{17}$$

$$H^*\psi^* = \Sigma_d \text{ in } V_d. \tag{18}$$

Supposing there is an arbitrary detector placed in a volume, the forward response can be obtained by

$$R = \iiint \Sigma_{\mathrm{d}}(r, E)\psi(r, E, \Omega) \mathrm{d}\,\Omega \mathrm{dEdV} \tag{19}$$

and commutation of equation (17) and equation (18) yields

$$\langle \psi^*, H\psi \rangle - \langle \psi, H^*\psi^* \rangle = \langle \psi^*, q \rangle - \langle \psi, q^* \rangle. \tag{20}$$

This reduces to

$$\langle \psi, q^* \rangle = \langle \psi^*, q \rangle \tag{21}$$

and by definition

$$R = \langle \psi^*, q \rangle. \tag{22}$$

The source sampling is then driven by the biased pdf

$$\hat{\mathrm{q}}(r, E) = \frac{\phi^*(r, E)\mathrm{q}(r, E)}{\mathrm{R}} = \frac{\phi^*(r, E)\mathrm{q}(r, E)}{\iint \mathrm{q}(r, E)\phi^*(r, E)\, \mathrm{d}r\mathrm{d}E} \tag{23}$$

and the weight of each particle is given by

$$w_o = \frac{q}{\hat{q}} \tag{24}$$

with consistent weight windows set up for the rouletting and splitting of particles [8].

1.5.2.1. Denovo

Shift implements CADIS based on a deterministic adjoint calculation provided by Denovo. Denovo itself is a 3D discrete ordinates transport code which provides forward and adjoint capability. The coupling used to generate the adjoint for CADIS, restricts many features of Denovo to gain efficiency. As a result, the solver solves transport on a relatively coarse cartesian grid, with an arbitrary number of energy groups and angles. Since the focus is on obtaining reliable estimations of the adjoint fluxes, Denovo utilizes step-characteristics spatial differencing. This choice guarantees that the adjoint flux is positive if the source is positive, which is an essential requirement for constructing the biasing associated with CADIS. Further details on Denovo are beyond its use here and are deferred to [9].

2. RESEARCH STATEMENT

The unique coupling that exists between MPACT and Shift places it in the unprecedented position of being able to quickly and independently compute the fission source, adjoint, and detector response from a single input. Having this ability makes it well positioned to conduct this study, since all the pieces needed for comparison are immediately made available. MPACT has been shown to accurately solve for the principal eigenvalue and associated eigenvector in many common benchmarks. It has also held up to benchmarking against the reactor data which it seeks to simulate [10]. Shift has also been found to be efficient and accurate when it has been compared to benchmarks problems. The coupled program has been tested for detector response calculations and found to agree quite well with MCNP [11].

With Shift modeling the detector response, this provides the key reference point needed to conduct a study of deterministically driven response estimation. As can be seen from equation (22) the detector response can be generated by the inner product of the adjoint flux and the fission source. However, the adjoint is typically not solved well enough for this reciprocity to be valid. In large part, because the adjoint problem is just as difficult to solve as the forward problem. However, establishing an algorithm which can closely approximate the detector response over a band of conditions is within reason.

2.1. Development

To begin the algorithm, the fission source for a fuel volume is defined as

$$\mathrm{q}(r,E)=\chi(r,E)\iint_0^\infty \nu\Sigma_\mathrm{f}(r',E')\phi(r',E')\mathrm{d}E'\mathrm{dV}' \tag{25}$$

and the power for the same fuel volume is given by

$$\mathrm{P}(r)=\iint_0^\infty \kappa\Sigma_\mathrm{f}(r',E')\phi(r',E')\mathrm{d}E'\mathrm{dV}'. \tag{26}$$

Dividing the left-hand side of equation (26) by the right-hand side and multiplying it with equation (25) yields

$$\mathrm{q}(r,E)=\frac{\mathrm{P}(r)\chi(r,E)\iint_0^\infty \nu\Sigma_\mathrm{f}(r',E')\phi(r',E')\mathrm{d}E'\mathrm{dV}}{\iint_0^\infty \kappa\Sigma_\mathrm{f}(r',E')\phi(r',E')\mathrm{d}E'\mathrm{dV}}. \tag{27}$$

Multiplying the bottom and top of equation (27) by the total neutron flux in the given volume

$$\frac{\iint_0^\infty \phi(r', E')\mathrm{d}\, E'\mathrm{d}V}{\iint_0^\infty \phi(r', E')\mathrm{d}\, E'\mathrm{d}V}$$

gives

$$q(\mathrm{r}, E) = \frac{\mathrm{P(r)}\chi(\mathrm{r}, E) \iint_0^\infty \nu\Sigma_\mathrm{f}(\mathrm{r}', E')\phi(\mathrm{r}', E')\mathrm{d}E'\mathrm{dV}}{\iint_0^\infty \kappa\Sigma_\mathrm{f}(\mathrm{r}', E')\phi(\mathrm{r}', E')\mathrm{d}E'\mathrm{dV}} \cdot \frac{\iint_0^\infty \phi(r', E')\mathrm{d}\, E'\mathrm{d}V}{\iint_0^\infty \phi(r', E')\mathrm{d}\, E'\mathrm{d}V}. \tag{28}$$

considering only a fuel volume and utilizing equation (7)

$$\frac{\iint_0^\infty \nu\Sigma_\mathrm{f}(\mathrm{r}', E')\phi(\mathrm{r}', E')\mathrm{d}E'\mathrm{dV}}{\iint_0^\infty \phi(r', E')\mathrm{d}\, E'\mathrm{d}V} = \overline{\nu\Sigma_f}(\mathrm{r}) \tag{29}$$

$$\frac{\iint_0^\infty \kappa\Sigma_\mathrm{f}(\mathrm{r}', E')\phi(r', E')\mathrm{d}\, E'\mathrm{d}V}{\iint_0^\infty \phi(r', E')\mathrm{d}\, E'\mathrm{d}V} = \overline{\kappa\Sigma_f}(\mathrm{r}) \tag{30}$$

which gives the energy dependent fission source for each fuel volume considered as a function of the power generated in that fuel volume

$$q(\mathrm{r}, E) = \frac{\chi(\mathrm{r}, E)\mathrm{P(r)}\overline{\nu\Sigma_f}(\mathrm{r})}{\overline{\kappa\Sigma_\mathrm{f}}(\mathrm{r})}. \tag{31}$$

Combining this with equation (22) and applying the definition of the inner product

$$\mathrm{R} = \int \int_0^\infty \chi(\mathrm{r}, \mathrm{E})\phi^*(r, E) \frac{\mathrm{P(r)}\overline{\nu\Sigma_f}(r)}{\overline{\kappa\Sigma_\mathrm{f}}(r)}\, \mathrm{d}\, E\mathrm{d}V. \tag{32}$$

In the case that fission is predominately in uranium 235, its fission spectrum can be used without sacrificing much accuracy. This will allow removing spatial dependence from fission spectrum. Implementing this simplification and rearranging yields

$$R = \int \frac{P(r)\overline{\nu\Sigma_f}(r)}{\overline{\kappa\Sigma_f}(r)} \int_0^\infty \chi(E)\phi^*(r,E)\ dE dV. \tag{33}$$

It should be noted that is only when the core is comprised completely of fresh fuel. If any of the fuel has been depleted, then this assumption is only a valid approximation if and only if: most of the fission occurs from uranium 235 and the energy groups are sufficiently wide to effectively mask subtle fission spectrum changes.

This can be discretized in energy with

$$\int_0^\infty \chi(E)\phi^*(r,E)dE \approx \sum_{g=1}^{G} \chi_g \phi_g^* \Delta E \tag{34}$$

where the term inside the volume integral represents the contribution to detector response from a given fuel volume so remaining integration is just over the number of such volumes within the core, which results in

$$R = \sum_{i=1}^{N} P_n \frac{\overline{\nu\Sigma_f}_n}{\overline{\kappa\Sigma_f}_n} \sum_{g=1}^{G} \chi_g \phi_{g,n}^* \Delta E. \tag{35}$$

This results in the calculation of total detector response based on parameters in discrete fuel volumes throughout the core. Taking each of these volumes to be a pin segment, as is modeled in MPACT, each of these quantities can be interpreted as pin segment average values. The power in each of these segments is often reported as a normalized quantity. In MPACT, this can be represented as

$$P_n = p_n h_n \bar{q} \tag{36}$$

where,

$P_n \equiv$ normalized pin powers

$p_n \equiv$ *absolute power generated*

$h_n \equiv$ *height of pins*

$\bar{q} \equiv$ *average linear heat rate* .

Giving rise to the final form;

$$R = \bar{q} \sum_{i=1}^{N} p_n h_n \frac{\overline{\nu\Sigma_f}_n}{\overline{\kappa\Sigma_f}_n} \sum_{g=1}^{G} \chi_g \phi^*_{g,n} \Delta E. \tag{37}$$

2.2. Approach

Every quantity that is to be utilized is the result of a series of approximations. However, MPACT has been shown to reliably calculate pin power [10]. It is assumed, that the cross sections can then be obtained from MPACT with reasonable accuracy based on trusted solution data and rigorous mathematical relations. This then implies that the detector response accuracy, of equation (37) is driven by the accuracy of the adjoint obtained by Denovo. This can then be compared to the benchmarking value provided by the Shift solution at the same set of conditions. This can then provide guidance for which parameters are required in the adjoint solution to adequately model detector responses.

3. NUMERICAL VERIFICATION

The base model for this study is a small modular reactor (SMR) based on an approximation the of NuScale reactor [12]. The full model is comprised of 37 fuel assemblies each measuring 200 cm in height, with a full model height of 240 cm. Many of the remaining parameters are based on a typical pressurized water reactor. The model has been simplified for this section by removing spacer grids and coarsening the axial levels to 10 cm each. It is also rotational symmetric and only a quarter core is simulated. A 10 cm tall detector is bisected by fuel midline and located 45 degrees from the azimuthal line of symmetry. For details on the general input see Appendix A.

3.1. Parameter Selection

From equation (37) the average linear heat rate functions as a proportionality constant if all other factors are solved exactly. However, it is known that all factors contain a degree of approximation and so this factor will not be produced exactly. Despite this fact, the proportionality factor that is obtained should tend toward a scalar value as the adjoint is approximated with increasing accuracy.

3.1.3. Energy Structure

It is anticipated that the thermal groups contribute far less to detector response than the fast groups. This relates to the notion that thermal groups encounter significantly more mean free paths than fast groups when transiting between the core periphery and detector. This should then increase the effective removal of slower neutrons, resulting in lower adjoint fluxes for slower groups and subsequently lower response contribution. This is then exacerbated by folding in the fission spectrum as in equation (37). Since the fission spectrum is peaked near the 2 MeV range, this makes these groups even more important to the overall contribution.

As a result of this logic, the group structure is refined mostly in the fast groups. Then for each calculated adjoint, the detector response is estimated with the corresponding fission source. The ratio the response calculated by Shift to the adjoint estimated response corresponds to the proportionality constant for the given conditions. A study of group structure effects on the adjoint response is conducted at a base moderator temperature of 220 C. The data shown in Figure 1, demonstrates that this proportionality constant approaches a number in the vicinity of 100 as the groups are refined. Due to relative crudeness of the adjoint at this point, the actual magnitude of this value is believed to be largely irrelevant. The important thing to note is that converging behavior is displayed, and this helps to demonstrate the extent to which the group structure is making significant impacts on the estimated response.

The remainder of this study will focus on the 3 “most converged” energy discretization. These structures are 36-groups, 48-groups, and 68-groups with bounds presented in Appendix B, Appendix C, and Appendix D, respectively. It is also worth noting that the 48-group library attempts to approximate the Bugle-96 library which has been shown to provide adequate results in excore transport simulations [13]. For this reason, the 48-group library which attempts to approximate it, will be used for gathering results while varying the remaining parameters.

3.1.4. Quadrature Order

Since the adjoint computation is based on the discrete ordinate method, it is susceptible to so-called ray effects. These effects can manifest as non-physical flux oscillations and/or artificially high flux contributions in mesh elements along the discrete direction [14]. The localized nature of the detector presents challenges in terms of ray effects for many quadrature sets. As a general strategy quadruple-range (QR) quadrature are used in lieu of level-symmetric and others due to previous experience showing improved performance in many cases [15] [16]. For this study, the QR orders used differ from Level Symmetric only in the quadrature weights.

Figure 2 displays the fastest group adjoint flux for the fuel midplane, with the approximate detector location annotated in the lower right-hand corner. While in Figure 3 the axial adjoint flux distribution is shown for assembly K-6 pin 17,17 (lowest-rightmost pin). As can be seen from Figure 2, this assembly is located along the 45-degree line which places the corner pin very near the detector which is located in the bottom right of the figure. Even under such proximity, flux oscillations are evident with the QR8, notably a double peak around the height of the detector which is located in the middle of the right edge of Figure 3. Figure 4 shows less extreme but still notable flux oscillations for Assembly L-7 with the QR8 quadrature. This type of oscillation is found in most pins across the core, albeit with lower peaks. In contrast the QR16 and QR32 quadrature show good agreement and are generally smooth about the axial height of the core. Due to the oscillations of QR8 and the agreement between QR32 and QR16 it is QR16 that will be used for further study.

3.1.5. Scattering Moments

The effect of scattering moments is made evident by the flux distribution between energy groups. For this reason, a similar approach to the one presented in section 3.1.3 is utilized for observing effects on the adjoint approximation.

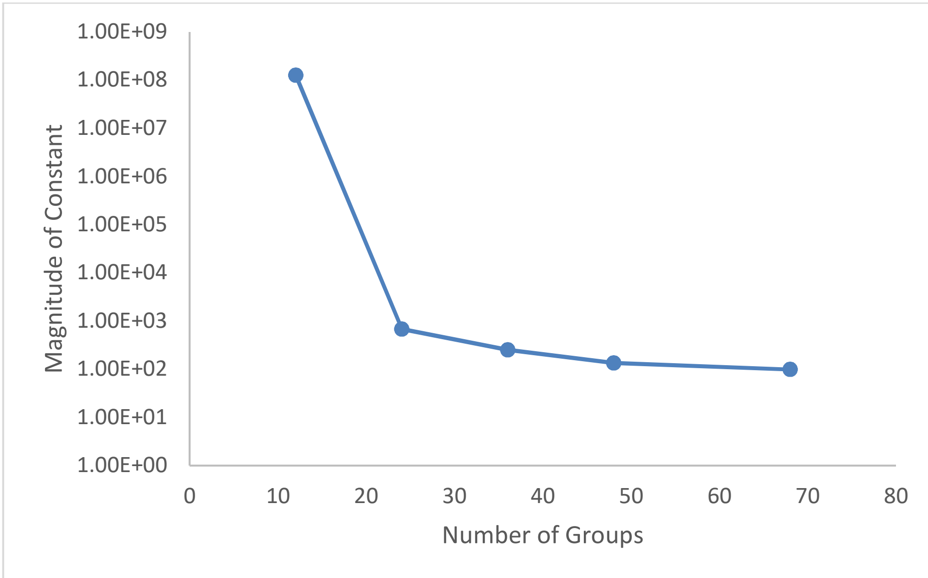

Figure 1: Effect of Energy Structure on Proportionality Constant

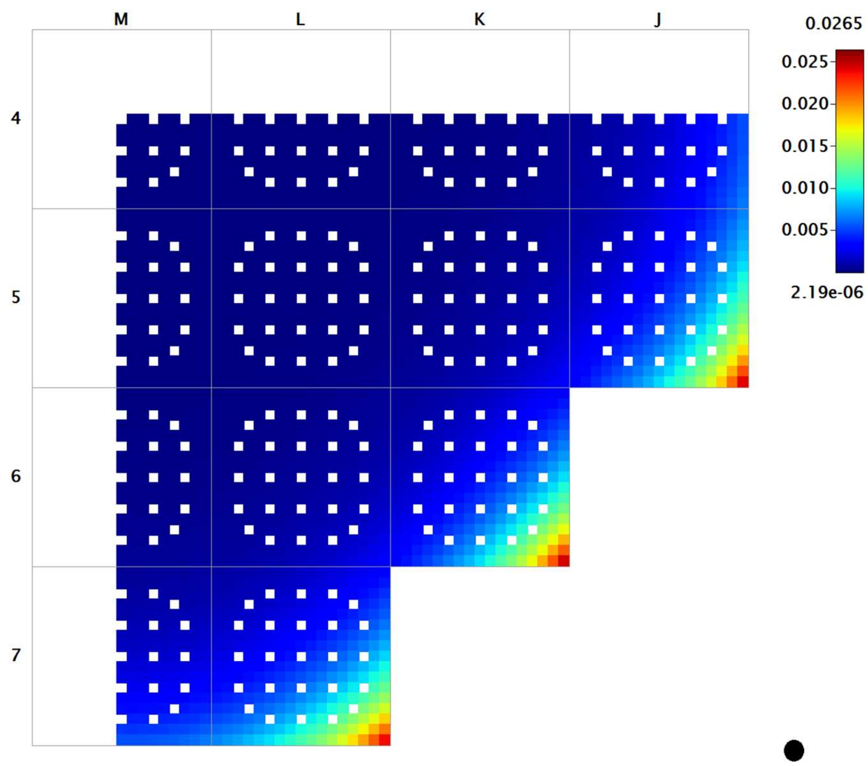

Figure 2: Adjoint Flux Fastest Group

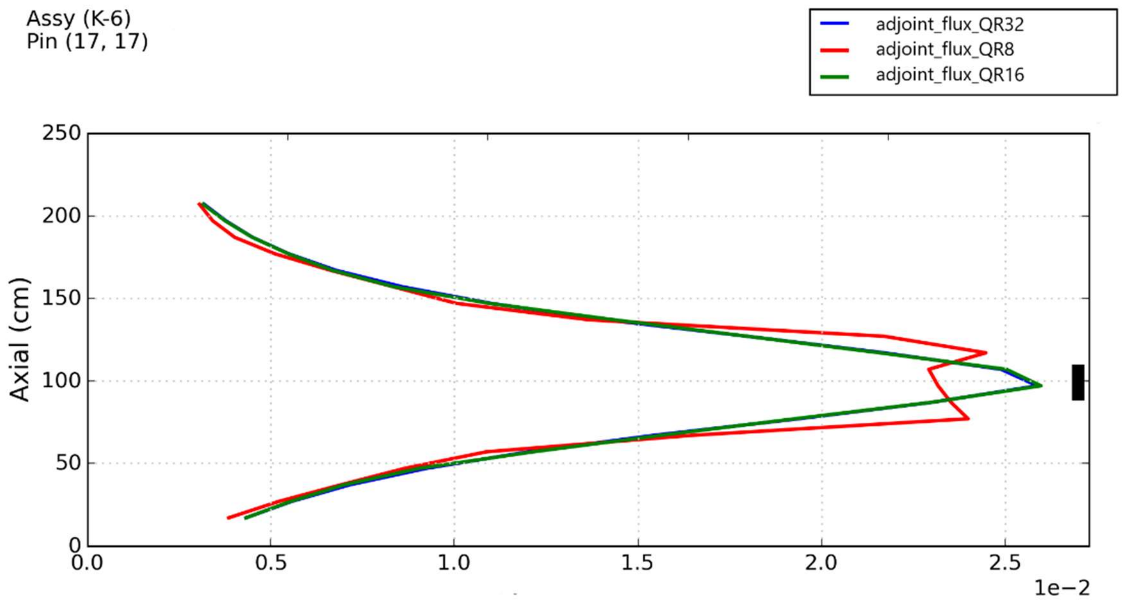

Figure 3: Axial Adjoint Flux Distribution for Assembly K-6 Pin 17,17

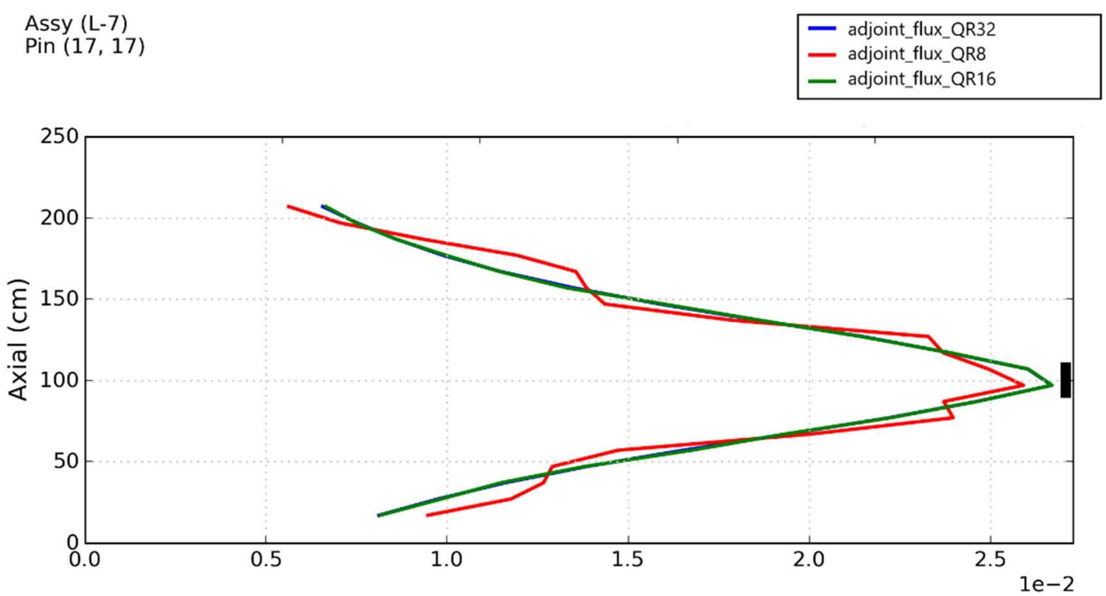

Figure 4: Axial Adjoint Flux Distribution for Assembly L-7 Pin 17,17

Since the idea is to constrain the error associated with the adjoint, the absolute magnitude of the proportionality constant is of little concern compared to the magnitude of changes between different parameterizations. Keeping this in mind, Figure 5 illustrates a noticeable change in the calculated factors between the P0 and P1 scattering moments. This suggests that the P0 approximation potentially introduces significant uncertainty in the adjoint.

Meanwhile, Figure 6 demonstrates good agreement between P3 and P1 approximations with a percent difference of only about 3% and about a half percent between P2 and P3 approximations. For the purposes of this study the 3 percent difference is sufficiently small that the decreased computational cost of P1 is favored. However, it is possible that utilizing P3 moments could allow for reducing the number of groups without sacrificing accuracy.

3.1.6. Mesh Size

While it is expected that the mesh size will have to be dramatically reduced in order to approach reciprocity, this option is not something that can be changed in the current coupling configuration. As a result, only one mesh element in the x-y plane is assigned to each pincell for this study. This limitation is expected to increase the adjoint error as a result of the assumptions made during pin homogenization. The axial meshing can be controlled through input, but since the x-y meshing parameters cannot be changed examination of the axial meshing effects on adjoint response is deferred to a later study.

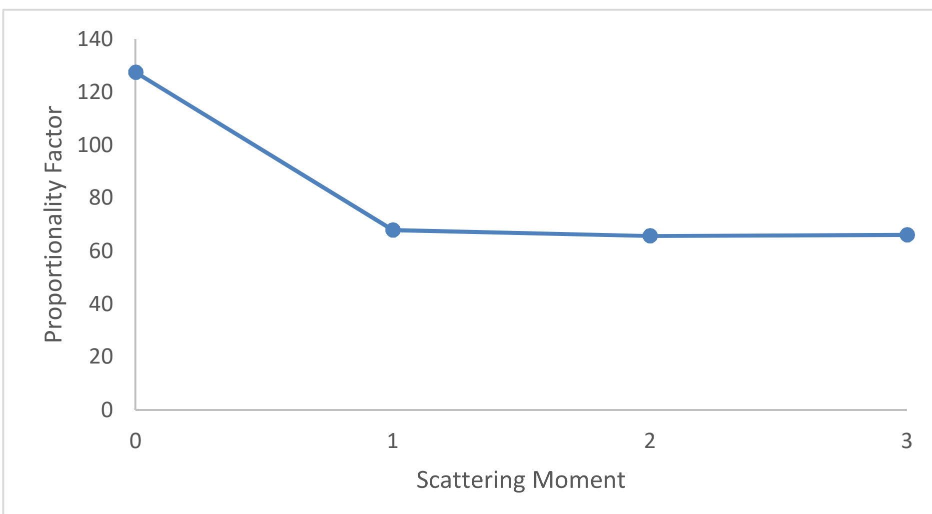

Figure 5: Scattering Moment Effect of Proportionality Constant

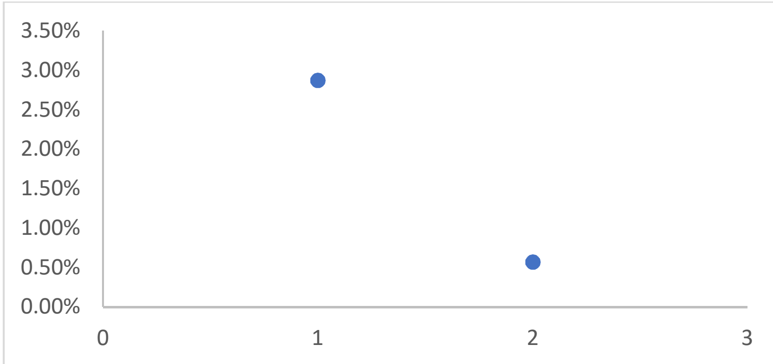

Figure 6: Percent Difference of P1 and P2 Moments Compared to P3

3.1.7. Parameter Summary

Methodically constraining approximations made in the adjoint calculation appear to suggest that using an adjoint calculated with 48-groups, utilizing QR16 quadrature, and P1 scattering provides a sufficiently converged solution that can then be used for making response estimations. By running a set of cases at varying moderator temperatures a range of proportionality constants can be obtained and averaged. This averaged proportionality can then be used in place of $\bar{q}$ from equation (37) to obtain an estimate of the absolute detector response.

The results shown in Figure 7, demonstrate good agreement between the adjoint based estimation and the monte carlo results for 5 benchmark moderator densities. Figure 8 percent differences displayed in Figure 8, demonstrate just how close the approximation is to the monte carlo benchmark. The most substantial difference is less than 5% at the highest moderator density sampled. There is also a noticeable step from positive to negative percent differences. The step change does not suggest that this effect is strictly related to stochastic variance, however the change is not large enough to completely rule it out either.

Given the reasonable agreement between the two methods at the chosen parameters, it is possible that some of the parameters could be relaxed and provide an efficiency gain while not unduly penalizing accuracy. To accomplish this an arbitrary guide of limiting the percent difference to 10 percent is chosen. It is also reasoned that reducing the number of energy groups has the broadest implication for reducing computational requirements, and Figure 1 demonstrates that the relative impact should be minimal. The response estimations for the 36-group structure are provided in Figure 9 and the corresponding percent differences in Figure 10. Figure 11and Figure 12 show the estimated response and percent differences from the 24-group energy structure.

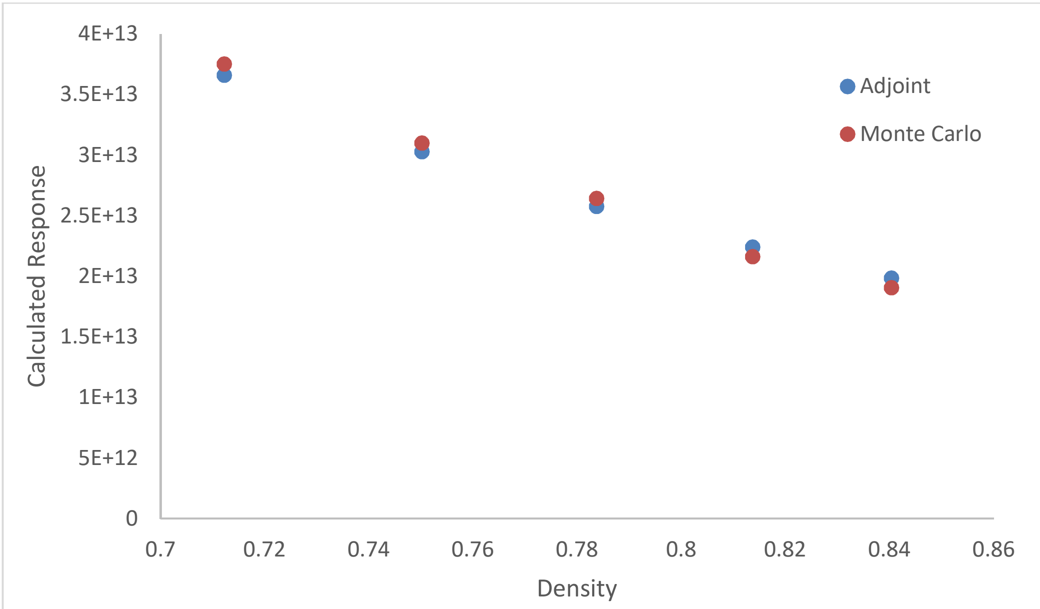

Figure 7: Comparison of Adjoint and Monte Carlo Response (48-groups)

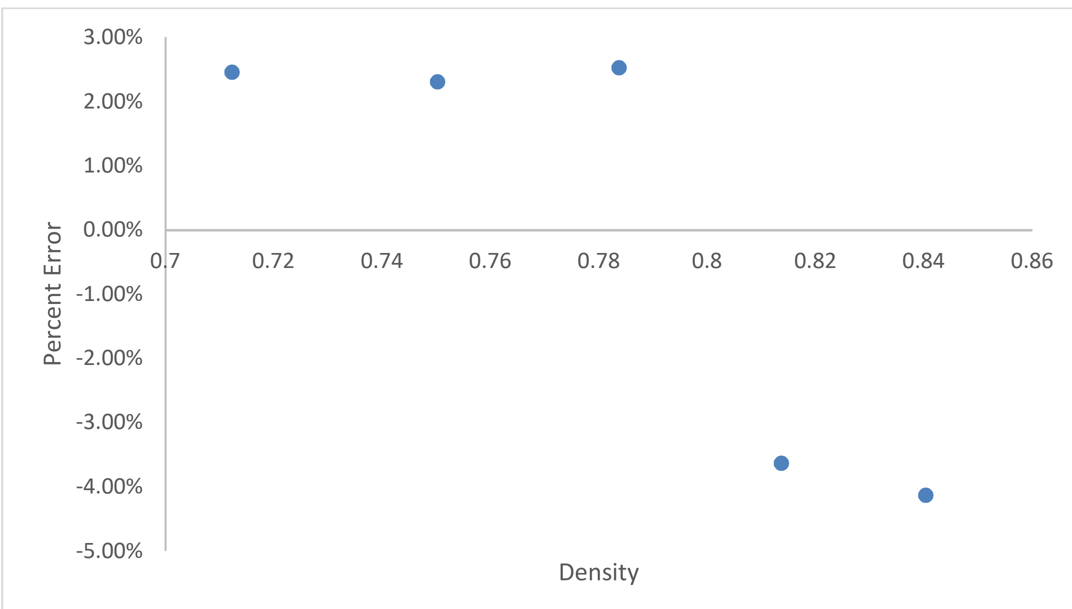

Figure 8: Adjoint and Monte Carlo Percent Difference(48-groups)

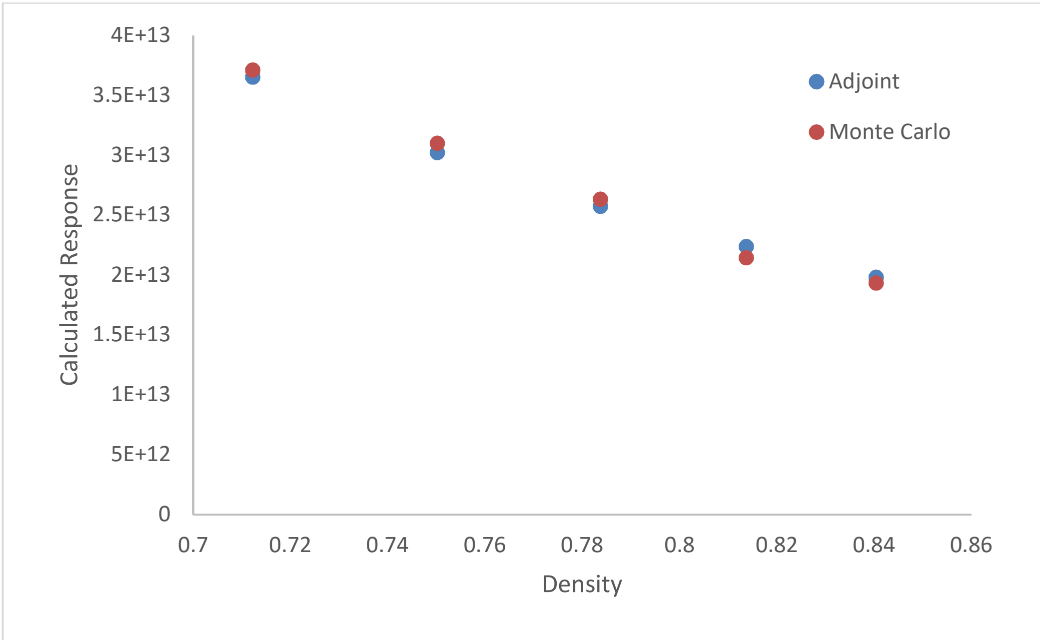

Figure 9: Comparison of Adjoint and Monte Carlo Response (36-groups)

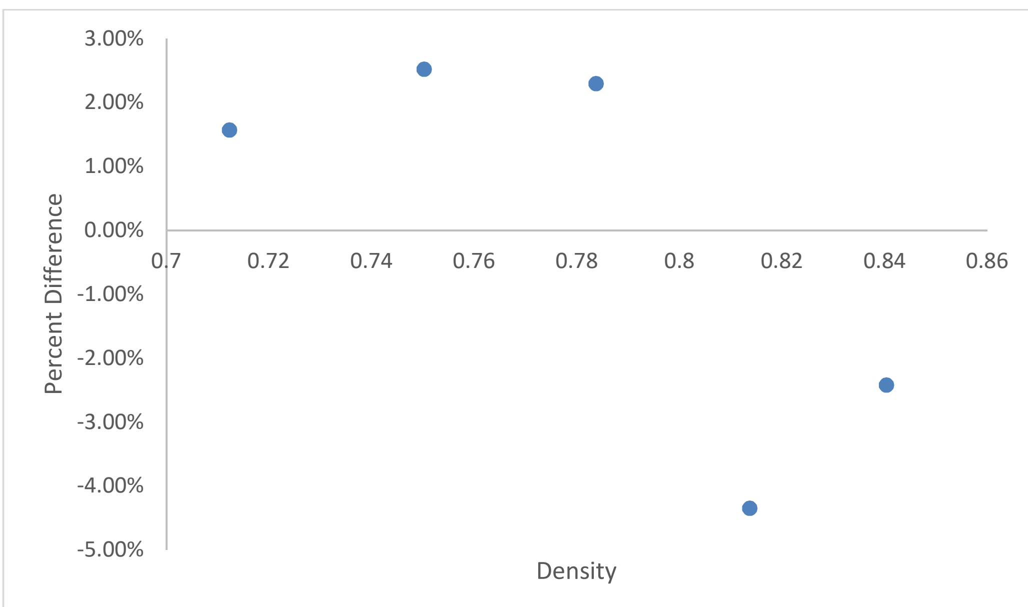

Figure 10: Adjoint and Monte Carlo Percent Difference (36-groups)

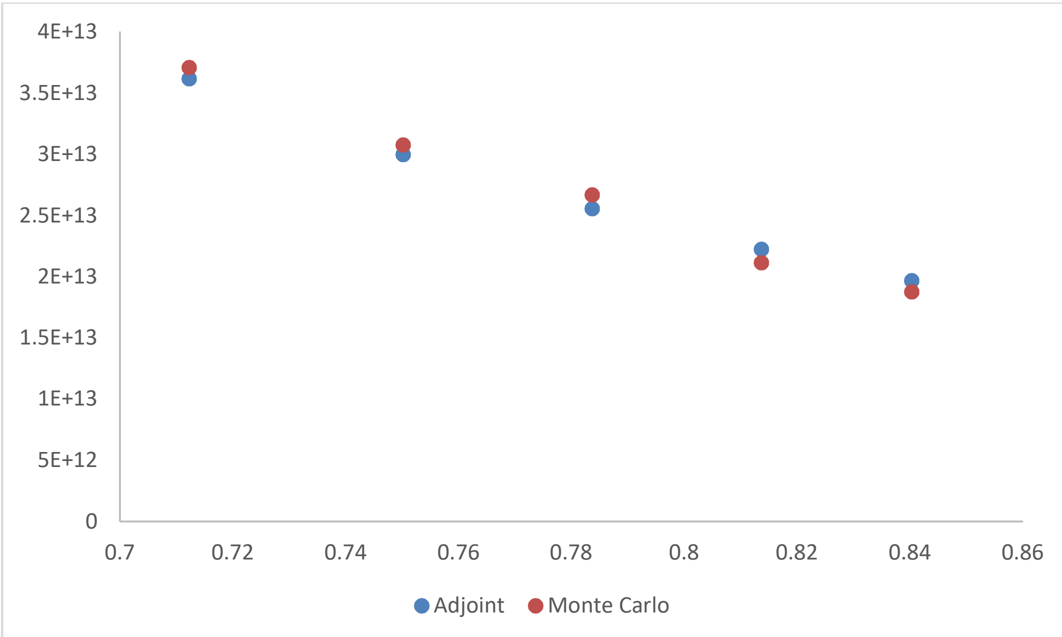

Figure 11: Comparison of Adjoint and Monte Carlo Response (24-Groups)

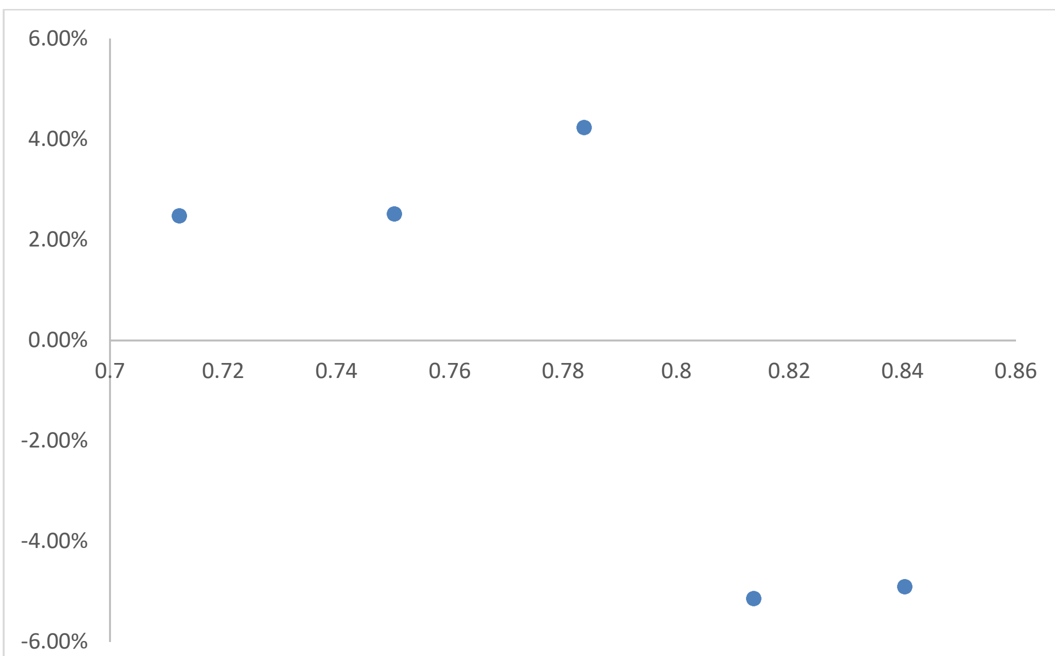

Figure 12: Adjoint and Monte Carlo Percent Difference (24-groups)

Comparison of Figure 7, Figure 9, and Figure 11 shows that the response estimates remain largely the same for all structures. While comparison of Figure 8, Figure 10, and Figure 12 shows that the percent differences also hold at not more than 5 percent for all structures considered.

However, the proportionality factors are based on stochastic results, and so the stochastic variance must be propagated through the calculated factors. This is a relatively straightforward process based on the definition of the proportionality factor; $Response/Adjoint = f$. From this definition the variance for f can then be approximated using a the Taylor series approach documented in [17]. This yields the following equation

$$\sigma_{\mathrm{f}}^2 = \mathrm{f}^2 \left(\frac{\sigma_{Response}}{Response}\right)^2. \tag{38}$$

Since the adjoint originates from a deterministic calculation its contribution to the variance of the factor is zero. This leaves the uncertainty in the stochastic response as the only contributor to uncertainty in the proportionality factors. The calculated average detector proportionality factors and standard deviation of those factors are presented in Table 1 across a range of densities and energy structures.

Inclusion of the standard deviations makes it possible to see the range of adjoint response estimations that could result from the subtle changes which are expected to occur with stochastic methods. These ranges are summarized in Table 2 as percentage the monte carlo modeled benchmarking result.

Table 1: Proportionality Factors with Propagated Uncertainty

Density	**48-group**	**36-group**	**24-group**
0.8403	68.00 ± 0.63	128.3 ± 1.8	349.0 ± 4.4
0.8136	68.33 ± 0.65	125.9 ± 1.3	348.2 ± 4.3
0.7837	72.64 ± 0.60	134.5 ± 1.3	382.3 ± 4.2
0.7502	72.48 ± 0.59	134.8 ± 1.2	375.6 ± 4.0
0.7123	72.59 ± 0.57	133.5 ± 1.2	375.4 ± 3.9
Average	70.81 ± 1.36	131.4 ± 3.0	366.1 ± 9.4

Table 2: Expected Maximum Percent Error Accounting for Variances

Density	48-group	36-group	24-group
0.8403	6.13	4.79	10.46
0.8136	5.62	6.76	10.71
0.7837	4.40	4.55	9.31
0.7502	4.19	4.77	7.69
0.7123	4.33	3.84	7.65

The factor variance of the 24-group increases the range in response uncertainty to as much as 10% of response. For this reason, it should serve as the minimum required structure, but in practical use the 36-group is suggested for this problem.

3.1.8. Applicability of Single Adjoint Weight Set

Equation (22) provides a method for estimating detector response provided a set of adjoint based weights and a fission source. However, the adjoint weights are based on the geometry and conditions present at the time the adjoint was calculated. To improve the usability of the adjoint, a method for extending the use of a single set of weights for a range of conditions. The most simplistic thing to change is the power level. However, in the absence of feedback, a change in power can be shown to provide a perfectly linear increase in response. This results from the power level being linearly proportional to the neutron flux level, and the response being proportional to the neutron flux leakage.

A more difficult case is that of changing moderator density. This has a demonstrable effect on the power distribution and the adjoint through changing neutron mean-free-paths (mfp) in the moderator. Simply changing one or the other is shown to be inadequate to capture the full effect of the density change on detector response. This prohibits accurately estimating response based solely on a single set of adjoint weights, demonstrated in Figure 13, which shows over 55% error between the estimated and the benchmark responses.

This can be accounted for by assuming the effects are separable, much like the effect of power level. Provided that the power distribution is captured in the forward solution then the remaining discrepancy must be a result of just the density. Table 3 shows the proportionality factors obtained using a single adjoint across multiple density dependent power distributions. The range of densities cover temperatures from roughly 200C through 325C

By assuming that the effects are separable, a shaping function based on density can be applied to incorporate the remaining affects. An exponential fit was chosen as it replicates the idea that neutron attenuation increases with the density of the water. Utilizing the factors arising from an exponential fitting of the calculated data points provides a method of scaling the detector response as a function of downcomer density. The error between the Shift solution and the estimated response are shown in Figure 14. From this it can be noted that the maximum difference is only 7% with a mean difference of about 3.25% and covers a range in temperature that spans a significant operating range.

3.1.9. Usability

Calculating response from the adjoint and fission source is a straightforward integration and requires only a few moments to accomplish. The responses calculated using VERA, took approximately two hours to complete. However, a significant fraction of this time was spent reducing the variance which aided in suppressing the deviation in factors.

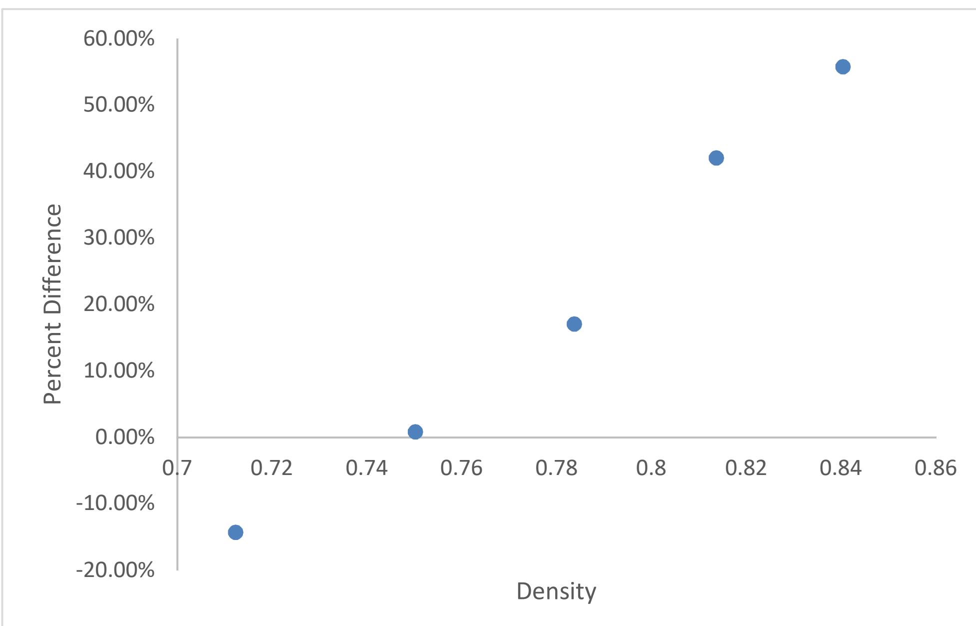

Figure 13: Percent Difference in Response From a Single Weight Set

Table 3: Comparison of Proportionality Factors

Density	Calculated	Exponential Fit
0.9588	33.42 ± 0.11	35.10
0.9166	43.40 ± 0.17	44.45
0.8643	59.93 ± 0.29	59.57
0.8403	73.44 ± 0.58	72.15
0.8136	80.53 ± 0.46	82.53
0.7837	97.72 ± 0.66	95.98
0.7502	113.52 ± 0.85	113.62
0.7122	133.52 ± 1.18	137.55
0.6545	187.50 ± 2.08	184.03

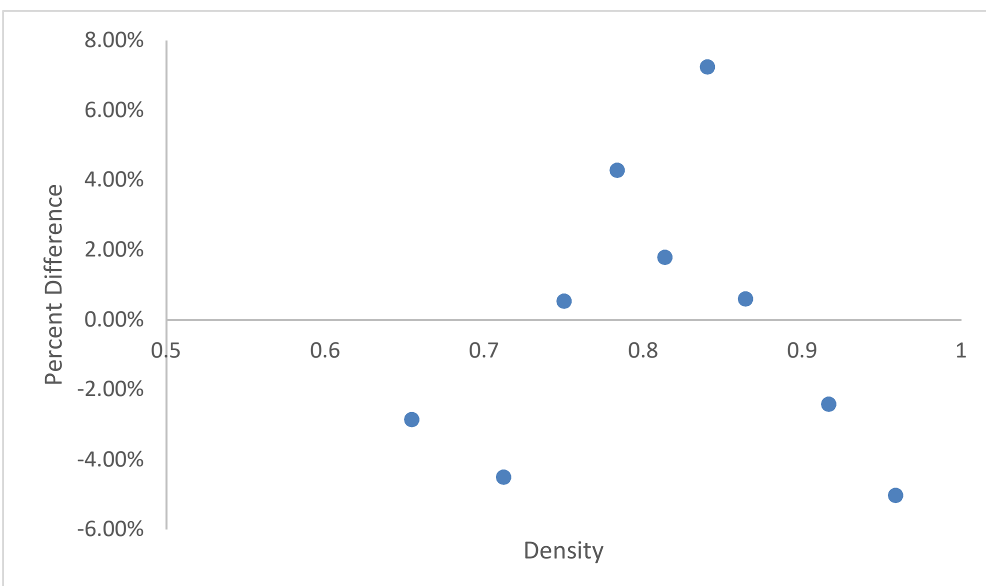

Figure 14: Error Between Estimated Response and Shift Result

4. CONCLUSIONS AND RECOMMENDATIONS

Throughout this study there has been an effort to restrict the introduction of errors to a practical extent. In particular, the general response estimator formulation is exact and the only introduced approximations through its components. Since most of the components can or have been benchmarked, this has enabled the focus on the adjoint itself and establishment of a guideline for choosing adjoint solution parameters for this geometry. This was then expanded to generate a weighting function that could be used to correct the adjoint weight for various densities under consideration.

This has demonstrated a reliable method for adjoint driven estimation of detector response which has been verified against Shift's independent calculation. While this was demonstrated with an SMR, adjoint methodology is robust to many reactor designs. It is also worth noting that the introduction of further errors is possible with the various forward solutions available. However, it is also shown through the derivation that the choice of volume integrals is largely arbitrary, which indicates that coarser power distributions could be utilized.

From this, two nominal use cases develop. The first invariant ex-core conditions with changing in-core conditions. The obvious case for this is changing fuel loading strategies. For this scenario a "base case" would be calculated, which would establish the adjoint to be utilized, then fuel shuffling would be performed. In this case, the detector could be a volume within the reactor vessel and would enable vessel flux minimization at key regions. For such a study it is possible that the weights could be collapsed over a broader region, i.e. nodes or assemblies. This would enable rapidly studying the effect of fuel pattern on vessel flux. Alternately, dynamic rod withdrawal would fit into the same approach. As would simply studying detector response for various power shapes.

Finally, this could also be utilized in simulation as a method for predicting detector response during other transients which do not affect downcomer density. Whereas the second method utilizes a single set of weights and a density dependent shaping function. This would be more applicable to transients which quickly change downcomer density. However, to fully account for such a transient would require considering feedback in the power shape, which is not explored here.

Further study is also still required to establish corresponding methods which account for perturbations beyond density. Most notably burnup, which challenges a preliminary assumption that the fission source is predominately uranium 235. Other conditions for further exploration include control rod position and the introduction of feedback mechanisms.

REFERENCES

[1] U.S. Nuclear Regulatory Commission, Westinghouse Technology Systems Manaul, 2011.

[2] Y. Shimazu, "Analytical Method for Recalibration of Incore and Excore Nuclear Instrumentation System of PWRs," *Journal of Nuclear Science adn Technology,* pp. 293-298, 1991.

[3] G. Farkas, J. Lipka, J. Hascik and V. Slugen, "Computation of Ex-Core Detector Weighting Funtions for VVER-440 Using MCNP5," in *Nuclear Energy for New Europe*, Bovec, Slovenia, 2011.

[4] Y. Zheng, D. Lee, P. Zhang and H.-c. Shin, "Comparisons of SN and Monte-Carlo methods in PWR ex-core detector response simulation," *Annals of Nuclear Energy,* pp. 139-150, 2017.

[5] J. A. Turner, K. Clarno, M. Sieger, R. Bartlett, C. Benjamin, R. Pawlowski, R. Schmidt and R. Summers, "The Virual Environment For Reactor Applications (VERA): Design and architecture," United States, 2016.

[6] T. Downar, B. S. Collins, J. C. Gehin and A. T. Godfrey, "MPACT Theory Manual," United States: N. p., 2016.

[7] T. Pandya, T. Evans, K. Clarno and B. Collins, "Excore Modeling with VERAShift," United States, 2018.

[8] A. Haghighat and J. Wagner, "Monte Carlo Variance Reduction with Deterministic Importance Functions," *Progress in Nuclear Engergy,* vol. 42, no. 1, pp. 25-53, 2003.

[9] T. M. Evans, A. S. Stafford, R. N. Slaybaugh and K. T. Clarno, "Denovo: A New Three-Dimensional Parallel Discrete Ordinates Code in SCALE," *Nuclear Technology,* vol. 171, no. 2, pp. 171-200, 2010.

[10] A. Godfrey, B. Collins, C. Gentry, S. Stimpson and J. Ritchie, "Watts Bar Unit 2 Startup Results with VERA," 2017.

[11] A. Godfrey, E. Davidson, G. Wolfram, B. Collins, C. Gentry, G. Ilas, S. Palmtag, T. Pandya and K. Royston, "Watts Bar Unit 1 Source Range Detector Response Validation During Refueling," 2019.

[12] NuScale Power, LLC, "Final Safety Analysis Report (FSAR) Rev.2," 2018.

[13] J. E. White, D. T. Ingersoll and R. W. Roussin, "BUGLE 96: A revised multigroup cross section library for LWR applications based on ENDF/B-VI Release 3," United States, 1996.

[14] J. J. Duderstadt and W. R. Martin, Transport Theory, New York, NY: John Wiley & Sons, 1979.

[15] I. K. Abu-Shumays, "Angular quadratures for improved transport computations," 1999.

[16] J. J. Jarrel, M. L. Adams and J. M. Risner, "Application of Quadruple Range Quadratures to Three-Dimensional Model Shielding Problems," *Nuclear Technology,* vol. 186, no. 2, pp. 424-430, 2009.

[17] E. S. Lee and R. N. Forthofer, Analyzing Complex Survey Data, 2nd ed., Thousand Oaks: Sage Publications, 2005.

APPENDIX

Appendix A. Generic SMR Input

```
[CASEID]
  title 'Small Modular Reactor - 7x7 Design - Public'

[STATE]
  power       100.0                           ! %
  tinlet      220 C                           ! inlet temp (F,K, or C)
  modden      0.840336
  boron       1000                            ! ppmB
  rodbank     A 200 B 200                     ! steps withdrawn
  sym         qtr
  excore_transport on
  edit pin_avgNuFiss pin_avgKappaFiss
  deplete EFPD 0.0

[CORE]
  size    7
  rated   160.0  4.7620                      ! power (MW), flow (Mlbs/hr)
  apitch  21.504                             ! cm
  height  240.0                              ! cm
  xlabel  R P N M L K J
  ylabel  1 2 3 4 5 6 7

  core_shape
    0 0 1 1 1 0 0
    0 1 1 1 1 1 0
    1 1 1 1 1 1 1
    1 1 1 1 1 1 1
    1 1 1 1 1 1 1
    0 1 1 1 1 1 0
    0 0 1 1 1 0 0

  assm_map
    1
    2 1
    1 2 3
    3 3

  insert_map
    -
   24  -
    - 16  -
    8  -

  det_map
    1
    -  1
    1  -  1
    -  1
```

```
  crd_map
    1
    - 1
    1 - 1
    - 1

  crd_bank
    A
    - B
    A - B
    - B

  baffle   ss 0.19 2.85                    ! gap, thickness (cm)

  vessel  mod 93.980                       ! barrel IR (cm)
           ss 99.060                       ! barrel OR (cm)
          mod 121.920                      ! vessel liner IR (cm)
           ss 122.555                      ! vessel liner OR (cm)
           cs 133.350                      ! vessel OR (cm)

  bioshield void 220.98
              ss 228.6
              cs 230.60
             mod 300.0

  det PWR power 8.75 9.5 / void cs / 10.0 / b10 none

  det_locations PWR 135.0 315 95.0

  lower_plate ss  5.0 0.5              ! mat, thickness (cm), vol frac
! upper_plate ss  7.6 0.5              ! mat, thickness (cm), vol frac

[ASSEMBLY]
  title  "SMR 2-meter 17x17 bundle"
  npin   17
  ppitch 1.260                             ! cm

  fuel U18 10.257 94.5 / 1.870             ! axial blanket

  cell b     0.4096 0.418 0.475 / U18 he zirc4       ! blanket cell
  cell G            0.561 0.602 / mod    zirc4       ! guide tube
  cell 5            0.418 0.475 /     he zirc4       ! plenum
  cell P                  0.475 /        zirc4       ! end plug
  cell X                  0.475 /        mod         ! gap

  lattice LAT18
    G
    b b
    b b b
    G b b G
    b b b b b
```

```
    b b b b b G
    G b b G b b b
    b b b b b b b b
    b b b b b b b b b

  lattice PLEN
    G
    5 5
    5 5 5
    G 5 5 G
    5 5 5 5 5
    5 5 5 5 5 G
    G 5 5 G 5 5 5
    5 5 5 5 5 5 5 5
    5 5 5 5 5 5 5 5 5

  lattice PLUG
    G
    P P
    P P P
    G P P G
    P P P P P
    P P P P P G
    G P P G P P P
    P P P P P P P P
    P P P P P P P P P

  lattice GAP
    G
    X X
    X X X
    G X X G
    X X X X X
    X X X X X G
    G X X G X X X
    X X X X X X X X
    X X X X X X X X X

  axial  1  6.0 GAP 8.0 PLUG 11.951 LAT18 211.951 PLEN 228.0 GAP 231.2
  axial  2  6.0 GAP 8.0 PLUG 11.951 LAT18 211.951 PLEN 228.0 GAP 231.2
  axial  3  6.0 GAP 8.0 PLUG 11.951 LAT18 211.951 PLEN 228.0 GAP 231.2

  lower_nozzle  ss 6.0 6250.0     ! mat, height (cm), mass (g)
  upper_nozzle  ss 8.8 6250.0     ! mat, height (cm), mass (g)

[INSERT]
  title "Pyrex"
  npin 17

  cell 1  0.214 0.231 0.241 0.427 0.437 0.484 / he ss he pyrex he ss
  cell P  0.214 0.231             0.437 0.484 / he ss          he ss
```

```
lattice  PY8
  -
  - -
  - - -
  1 - - -
  - - - - -
  - - - - - 1
  - - - - - - -
  - - - - - - - -
  - - - - - - - - -

lattice  PY12
  -
  - -
  - - -
  1 - - -
  - - - - -
  - - - - - -
  - - - 1 - - -
  - - - - - - - -
  - - - - - - - - -

lattice  PY16
  -
  - -
  - - -
  1 - - -
  - - - - -
  - - - - - 1
  - - - 1 - - -
  - - - - - - - -
  - - - - - - - - -

lattice  PY20
  -
  - -
  - - -
  1 - - -
  - - - - -
  - - - - - 1
  1 - - 1 - - -
  - - - - - - - -
  - - - - - - - - -

lattice  PY24
  -
  - -
  - - -
  1 - - 1
  - - - - -
  - - - - - 1
  1 - - 1 - - -
```

```
  - - - - - - - -
  - - - - - - - - -

lattice  PL8
  -
  - -
  - - -
  P - - -
  - - - - -
  - - - - - P
  - - - - - - -
  - - - - - - - -
  - - - - - - - - -

lattice  PL12
  -
  - -
  - - -
  P - - -
  - - - - -
  - - - - - -
  - - - P - - -
  - - - - - - - -
  - - - - - - - - -

lattice  PL16
  -
  - -
  - - -
  P - - -
  - - - - -
  - - - - - P
  - - - P - - -
  - - - - - - - -
  - - - - - - - - -

lattice  PL20
  -
  - -
  - - -
  P - - -
  - - - - -
  - - - - - P
  P - - P - - -
  - - - - - - - -
  - - - - - - - - -

lattice  PL24
  -
  - -
  - - -
  P - - P
```

```
    - - - - -
    - - - - - P
    P - - P - - -
    - - - - - - - -
    - - - - - - - - -

  axial   8  15.817 PY8  211.951 PL8  231.2
  axial  12  15.817 PY12 211.951 PL12 231.2
  axial  16  15.817 PY16 211.951 PL16 231.2
  axial  20  15.817 PY20 211.951 PL20 231.2
  axial  24  15.817 PY24 211.951 PL24 231.2

[CONTROL]
  title "B4C with AIC tips"
  npin    17
  stroke  200.0  200          ! total stroke (cm), number of steps (1.0
cm/step)

  cell 1  0.382 0.386 0.484 / aic he ss
  cell 2  0.373 0.386 0.484 / b4c he ss

  lattice AIC
    -
    - -
    - - -
    1 - - 1
    - - - - -
    - - - - - 1
    1 - - 1 - - -
    - - - - - - - -
    - - - - - - - - -

  lattice B4C
    -
    - -
    - - -
    2 - - 2
    - - - - -
    - - - - - 2
    2 - - 2 - - -
    - - - - - - - -
    - - - - - - - - -

  axial  1    17.031
         AIC 118.631
         B4C 211.951

[EDITS]
  axial_edit_bounds
     11.951
     21.951
     31.951
```

```
     41.951
     51.951
     61.951
     71.951
     81.951
     91.951
     101.951
     111.951
     121.951
     131.951
     141.951
     151.951
     161.951
     171.951
     181.951
     191.951
     201.951
     211.951

[MPACT]
  num_space              108

[SHIFT]
  Np                     5e7
  fiss_src_spectrum      nuclide_watt
  num_blocks_i           6
  num_blocks_j           6
  core_translate         -99.060 -99.060 0.0
  excore_filename        smr.excore.xml
  xs_library             v7-252
  global_log             debug
! hybrid
  Pn_order               0
  Sn_order               8
  within_group_tolerance 1.0E-08
  upscatter_tolerance    1.0E-08
  iterate_downscatter    true
  output_adjoint         true
```

Appendix B. 36-Group Energy Bounds (MeV)

```
1.00E-05
1.00E-04
1.00E-03
1.00E-02
1.00E-01
1.00E+00
1.00E+01
1.01E+02
1.15E+03
5.70E+03
9.50E+03
1.70E+04
3.00E+04
5.00E+04
6.00E+04
7.50E+04
8.50E+04
1.28E+05
2.70E+05
4.00E+05
4.40E+05
5.50E+05
6.00E+05
6.79E+05
8.20E+05
8.75E+05
1.01E+06
1.20E+06
1.32E+06
1.50E+06
2.35E+06
2.48E+06
4.80E+06
6.43E+06
1.28E+07
1.57E+07
```

Appendix C. 48-Group Energy Bounds (MeV)

```
1.00E-05
1.00E-04
1.00E-03
1.00E-02
1.00E-01
1.00E+00
1.00E+01
1.01E+02
5.50E+02
1.15E+03
2.50E+03
9.50E+03
1.70E+04
2.00E+04
3.00E+04
5.00E+04
6.00E+04
7.30E+04
7.50E+04
8.50E+04
1.28E+05
2.00E+05
2.70E+05
3.30E+05
4.00E+05
4.40E+05
4.92E+05
5.50E+05
6.00E+05
6.79E+05
7.50E+05
8.20E+05
8.75E+05
9.20E+05
1.01E+06
1.20E+06
1.32E+06
1.40E+06
1.50E+06
1.85E+06
2.35E+06
2.48E+06
3.00E+06
4.30E+06
4.80E+06
6.43E+06
8.19E+06
1.28E+07
```

Appendix D. 68-Group Energy Bounds (MeV)

1.00E-05
1.00E-04
1.00E-03
1.00E-02
1.00E-01
1.00E+00
1.00E+01
1.01E+02
1.15E+03
3.90E+03
5.70E+03
8.03E+03
9.50E+03
1.30E+04
1.70E+04
2.00E+04
3.00E+04
4.50E+04
5.00E+04
5.20E+04
6.00E+04
7.30E+04
7.50E+04
8.20E+04
8.50E+04
1.00E+05
1.28E+05
1.49E+05
2.00E+05
2.70E+05
3.30E+05
4.00E+05
4.20E+05
4.40E+05
4.70E+05
4.92E+05
5.50E+05
5.73E+05
6.00E+05
6.70E+05
6.79E+05
7.50E+05
8.20E+05
8.61E+05
8.75E+05
9.00E+05
9.20E+05
1.01E+06
1.10E+06
1.20E+06
1.25E+06
1.32E+06
1.36E+06
1.40E+06
1.50E+06
1.85E+06
2.35E+06
2.48E+06
3.00E+06
4.30E+06
4.80E+06
6.43E+06
8.19E+06
1.00E+07
1.28E+07
1.38E+07

VITA

Shane C. Henderson was born September 10, 1986 in Independence, Kansas to Marilyn and Garry. He has three brothers: Justin, Nicholas, and Jarrod. Shane graduated from Independence Senior High School in 2005 joining the United States Navy as Nuclear Machinist Mate the same year.

He attended Navy Nuclear Power School in Charleston, South Carolina and Navy Nuclear Power Training Ballston Spa in Ballston Spa, NY. Following training, Shane was assigned to the USS Harry S. Truman (CVN 75) homeported in Norfolk, VA. During his time aboard ship, he served on two deployments in support of OEF/OIF. Shane earned an honorable discharge on June 14, 2011.

In 2006, while stationed in Ballston Spa, Shane met his wife Ginger. They were married in 2009. Welcoming their oldest son, Levi, in 2010. After leaving active service, they relocated to Raleigh, NC where they welcomed the second child, Nathaniel. During their time in North Carolina, Shane earned his bachelor's degree in Nuclear Engineering from NC State and Ginger earned her bachelor's degree in Business from East Carolina University.

Following graduation in 2017, they relocated to Knoxville, TN, welcoming their third child and only daughter, Ottilia in 2018. Since arriving in Knoxville Shane has been employed as an associate researcher at Oak Ridge National Lab and simultaneously pursued his master's degree at the University of Tennessee. Shane will graduate in August 2019 and would like to continue studying for a Ph.D. while actively working as a researcher